NUCL SCI TECH (2021) 32:72
https://doi.org/10.1007/s41365-021-00911-0

Theoretical analysis of long-lived radioactive waste in pressurized water reactor

Ze-Xin Fang[1] · Meng Yu[1] · Ying-Ge Huang[1] · Jin-Bei Chen[1] · Jun Su[1] · Long Zhu[1]

Received: 15 March 2021 / Revised: 7 May 2021 / Accepted: 13 May 2021 / Published online: 14 July 2021

Abstract

Background The accelerator-driven subcritical transmutation system (ADS) is an advanced technology for the harmless disposal of nuclear waste. A theoretical analysis of the ingredients and content of nuclear waste, particularly long-lived waste in a pressurized water reactor (PWR), will provide important information for future spent fuel disposal.

Purpose The present study is an attempt to investigate the yields of isotopes in the neutron-induced fission process and estimate the content of long-lived ingredients of nuclear waste in a PWR.

Method We combined an approximation of the mass distribution of five Gaussians with the most probable charge model (Z_p model) to obtain the isotope yields in the ^{235}U(n,f) and ^{239}Pu(n,f) processes. The potential energy surface based on the concept of a di-nuclear system model was applied to an approximation using five Gaussian functions. A mathematical formula for the neutron spectrum in a PWR was established, and sets of differential equations were solved to calculate the content of long-lived nuclides in a PWR.

Results The calculated isotopic fission yields were in good agreement with the experimental data. Except for ^{238}U, the contents of ^{239}Pu, ^{240}Pu, ^{241}Pu, ^{242}Pu, ^{237}Np, ^{235}U, and ^{236}U are predominant in the PWR after reaching a discharge burnup. In addition, some isotope pairs of heavy nuclei reach a similar value after stabilization, which can be explained by the decay chain and effective fission cross-sections. For fission fragments, we simulated the content evolution of some long-lived nuclides ^{90}Sr, ^{107}Pd,^{135}Cs, and their isobars ^{90}Rb, ^{107}Rh, and ^{135}Xe during a fuel cycle in a PWR. The variations in the inventories of uranium and plutonium were in good agreement with the data in Daya Bay.

Conclusion A new method is proposed for the prediction of the isotopic fission yield. The inventory of long-lived nuclides was analyzed and predicted after reaching a discharge burnup.

Keywords Radiotoxicity · PWR · Five Gaussians · Long-lived nuclides · Fission fragments yields

1 Introduction

With the development of the nuclear industry, the amount of radioactive waste in storage worldwide has rapidly increased. An efficient prediction of the composition of spent fuel in nuclear reactors plays an important role in the design of facilities for radioactive waste management and has been a topic of significant interest. In [1], formulas and basic data were proposed for calculating the fission product radioactivity for a thermal neutron reactor. Similarly, codes for the fission products in the primary loop of a

Ze-Xin Fang and Meng Yu have contributed equally to this work.

This work was supported by the National Natural Science Foundation of China (No. 11605296) and the Natural Science Foundation of Guangdong Province, China (No. 2016A030310208), and Fundamental Research Funds for Central Universities (No. 18lgpy87).

✉ Long Zhu
zhulong@mail.sysu.edu.cn

[1] Sino-French Institute of Nuclear Engineering and Technology, Sun Yat-sen University, Zhuhai 519082, China

pressurized water reactor (PWR) were developed [2, 3]. Simulations and calculations of the neutron flux densities have also been extensively studied [4–10].

In recent years, significant progress has been made in the mechanism of nuclear fission [11–18], which provides essential information for estimating the fission products in a nuclear reactor. The fission process can be described as a potential energy surface guiding the evolution of the nuclear shape [19, 20]. According to the scission model, the shell effects can be reflected in the fission yield and can be distinguished according to different fission modes, which is related to the deformation of the nucleus at the scission point [20, 21]. The improved scission-point model describes the charge distributions well [22]. The Gaussian fitting approach has been widely and successfully used in investigations into various fission products. By approximating different fission modes to Gaussian distributions, the dependence of the different fission modes on the mass and charge distributions can be studied. In general, the experimental data of a neutron-induced fission yield are measured with a fixed incident neutron energy within a certain energy range. Therefore, to study the continuous behavior of the fission yield with incident neutron energy, it is necessary to establish a continuous relationship between the yield and excitation energy. One of the most frequently adopted phenomenological approaches is to approximate the fission yield through a superposition of several Gaussian distributions [23]. However, most curve fitting results have been found through studies using a fixed neutron energy or specific compound nucleus. In this study, we theoretically analyse the evolution of fission products in a PWR using the multi-Gaussian function in combination with the most probable charge model and the concept of a di-nuclear system.

The calculations are based on the parameters and information of a typical domestic PWR. The neutron spectrum plays an important role in studies on the fission product yields in a reactor. Wigeland et al. [24] divided the neutron spectrum into two energy ranges: thermal and fast, depending on the incident neutron energy. The epithermal energy range is also defined to better describe the spectrum [25]. The semi-empirical method can be useful for determination of the neutron spectrum [26].

Figure 1 shows the neutron spectrums in different nuclear reactors. It can be seen that a general incident neutron energy range in a reactor varies from 0.001 eV to 10 MeV. The formula used in this study was established to calculate the fission yields within this energy range. As mentioned above, the fission process in a nuclear reactor produces substantial fission fragments, which influence the reactivity of the reactor. However, fissile nuclides in a nuclear reactor continuously produce large amounts of

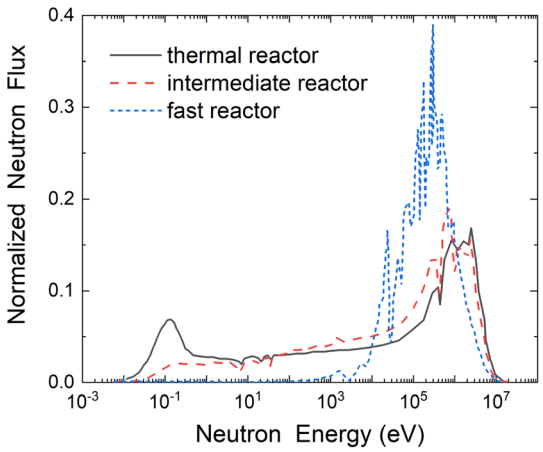

Fig. 1 (Color online) Neutron spectrums for thermal, intermediate, and fast reactors

long-lived nuclides, some of which, including ^{239}Pu, ^{241}Pu, and ^{233}U, can be extracted and reused in fission reactions [27, 28]. However, some fission fragments, such as ^{90}Rb, ^{107}Rh, and ^{135}Xe are highly radioactive. The transmutation of minor actinides also contributes to long-term radiotoxicity [29]. The ADS system is flexible for lowering such waste [30], and the storage of spent nuclear fuel should be considered crucial [31]. Therefore, it is necessary to investigate the properties of the fission fragment evolution in a PWR in a theoretical manner.

The remainder of this paper is organized as follows. In Sect. 2, the details of the theoretical method are described. The results and discussion are presented in Sect. 3. In Sect. 4, we provide some concluding remarks regarding this study.

2 Model

2.1 Multi-Gaussian functions

The Gaussian model was first proposed by Wahl [32], and this approach, based on the five Gaussians, has been widely used and continuously improved in estimations of fission fragment distributions. The expression for the five Gaussian superposition can be written as [33]:

$$y(A) = \sum_{i=1}^{5} \frac{Y_i}{\sqrt{2\pi}\sigma_i} \exp\left\{ -\frac{(A - \frac{A_F}{2} + \Delta_i + nt)^2}{2\sigma_i^2} \right\}, \quad (1)$$

where Y_i represents the proportion of each Gaussian component. In addition, σ_i and Δ_i are the Gaussian parameters, $2nt$ is considered as the total number of neutrons emitted during the fission process, and A_F is the mass of the compound nucleus.

Based on the symmetrical characteristic of the fission-fragment mass distribution with respect to $\frac{A_F}{2} - nt$, the relationship between the yields of light fragments and heavy fragments can be written as

$$y(Z_L, A_L) = y(Z_F - Z_L, A_F - 2nt - A_L) = y(Z_H, A_H), \tag{2}$$

where Z_L, A_L, Z_H, A_H, Z_F, and A_F denote the proton number, mass number of light fragments, heavy fragments, and compound nucleus, respectively. It is considered that $Y_1 = Y_5$, $Y_2 = Y_4$, $\Delta_1 = -\Delta_5$, $\Delta_2 = -\Delta_4$, $\Delta_3 = 0$, $\sigma_1 = \sigma_5$, and $\sigma_2 = \sigma_4$. The proportions of these Gaussian components, Y_i, are normalized such that $\sum_{i=1}^{5} Y_i = 2$. All of these Gaussian parameters are considered as functions of the excitation energy E^*.

2.2 Potential energy surface

The parameters Y_2 and Y_3 in Eqs. (1) influence the variation tendency of the peak-to-valley ratio $\frac{y_{peak}}{y_{valley}}$. In addition, y_{peak} and y_{valley} represent the peak and valley in the mass distribution for the product yields, respectively. Normally, the potential energy surface reflects the fission probability. Figure 2 shows the potential energy surface of ^{235}U in the di-nuclear system (DNS) concept, which is defined as follows [34–37]

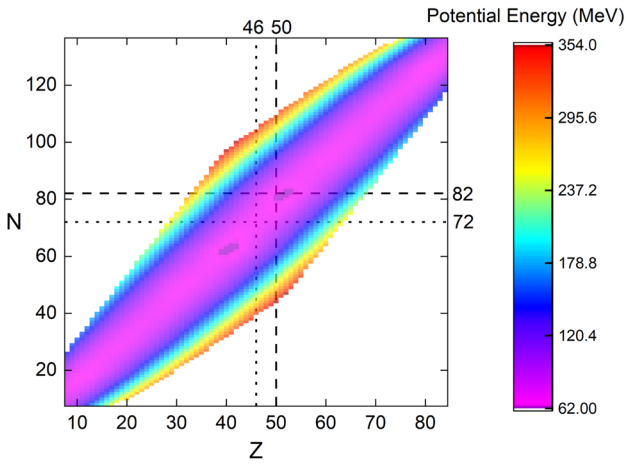

Fig. 2 (Color online) Potential energy surface for the reaction ^{235}U(n,f). The dashed and dotted lines indicate the fragment combinations with the minimum potential energy and the configuration in the symmetry fission, respectively

$$\begin{aligned} U(Z_i, N_i, R) =& U_L^{LD}(Z_L, N_L) + U_H^{LD}(Z_H, N_H) - U_{CN}^{LD} \\ &+ \delta U_L^{shell}(Z_L, N_L) + \delta U_H^{shell}(Z_H, N_H) \\ &+ V^C(Z_i, N_i, R) + V^N(Z_i, N_i, R), \end{aligned} \tag{3}$$

where the indices i = L, H, and CN denote light, heavy, and compound nuclei, respectively. The potential energy is assumed to be the sum of the liquid drop (U_i^{LD}) and microscopic shell correction (δU_i^{shell}) for each DNS nucleus. In addition, the nuclear potential (V^N) and Coulomb potential (V^C) were used to describe the interaction between the fragments [34].

Relatively low potential energies result in high fission yields of the corresponding fragments [38–40]. Owing to shell closures of Z = 50 and N = 82, the valley with the minimum value V_{min} can be seen, which results in relatively high fission yields of approximately Z = 50 and N = 82. By contrast, the potential energy V_{mid} at the central position influences the fission yield at approximately Z = 46 and N = 72.

We assume that $\frac{Y_2}{Y_3}$ is related to the values of V_{mid} and V_{min} and can be written as

$$\frac{Y_2}{Y_3} = f(V_{mid} - V_{min}). \tag{4}$$

2.3 Nuclear charge distribution

To obtain the isotopic fission yield, it is also assumed according to the most probable charge model [41] that the fission yield in the isobaric chains with mass number A follows a Gaussian dispersion:

$$y(Z, A) = \frac{y_A}{\sqrt{2\pi}\sigma_Z} \exp\left(\frac{-(Z - Z_p(A))^2}{2\sigma_Z^2}\right), \tag{5}$$

where y_A and σ_Z are Gaussian parameters. In addition, $Z_p(A)$ is the most probable charge in isobaric chains with mass number A. In [19], the fission yield of full isotopes for a different fission system is studied. It was found that the $\frac{N}{Z}$ ratio of heavy fragments with the most probable charge is closer to the $\frac{N}{Z}$ value of the compound nucleus. Therefore, we use a linear relation to describe the position of the most probable charge in the isobaric chains:

$$Z_p = k(A - A_H) + b. \tag{6}$$

Considering the charge conservation and symmetry of the mass distribution, k and b are determined as follows:

$$k = \left(Z_F - \frac{2A_H Z_F}{A_F}\right)/(A_L - A_H), \tag{7}$$

$$b = \frac{A_H Z_F}{A_F}, \tag{8}$$

where A_L and A_H represent the mass numbers of light and heavy fragments, respectively. In an isobaric chain,

$$\sum_i y(Z_i, A) = y(A), \tag{9}$$

where $y(A)$ is the mass distribution and $y(Z_i, A)$ is the yield of the fission fragment with proton number Z_i in the isobaric chain with mass number A. The determination of parameter σ_Z involves the study of $\langle\sigma_Z\rangle$ and $\left\langle\sigma_Z^2\right\rangle$ for different fission systems. To make the formula more universal, σ_Z in Eq. (5) is replaced by the average value ($\langle\langle\sigma_Z\rangle\rangle$) for all isobaric chains, which results in the absence of odd-even effects. In addition, following the description in [42], for a different fission system, $\left\langle\sigma_Z^2\right\rangle$ is energy independent. In addition, for a compound nucleus with the same proton number, $\langle\sigma_Z\rangle$ can be assumed to be constant. In this study, $\langle\sigma_Z\rangle$ = 0.55 [42].

2.4 Prediction of components in spent fuel

The inventory of components in a PWR can be obtained through the following formula [43, 44]:

$$\frac{dN_i(t)}{dt} = \sum_l N_l(t)\cdot\sigma_{f,l}\cdot\Phi\cdot y_{i,l} + \sum_k \lambda_k \cdot K_{p,k}\cdot N_k(t) + \sum_j \sigma_{c,j}\cdot\Phi\cdot N_j(t) - \left(\lambda_i + \sigma_{a,i}\cdot\Phi\right)\cdot N_i(t), \tag{10}$$

where N_i is the nuclide number density of isotope i. In addition, $\sigma_{f,l}$, $\sigma_{c,j}$, and $\sigma_{a,i}$ represent the microscopic effective fission cross section, gamma capture cross section, and absorption cross section, respectively. Moreover, Φ denotes the neutron flux in the reactor, $y_{i,l}$ is the yield of fragment i produced by the fissile nuclide l, λ_i is the decay constant of nuclide i, and $K_{p,k}$ is the decay branching ratio of parent nuclide k. It can be seen that the production process of nuclide i contains several parts. For heavy nuclides, the formation from the decay process and neutron capture are considered. For fission fragments, the fission yield was also considered. The consumption process includes decay and neutron absorption.

The effective microscopic reaction cross section is defined as [43]

$$\sigma_{x,r} = \int_{0.001\text{eV}}^{10\text{MeV}} dE_n \sigma_{x,r}(E_n)\chi(E_n). \tag{11}$$

In the above equation, $\sigma_{x,r}$ is defined as the effective microscopic cross section for the reaction r of nuclide x. In addition, E_n is the neutron energy in the reactor, and χ is the neutron distribution probability density, which is simplified as space-independent. The integral bound at 10 MeV and 0.001 eV is determined based on the energy range of the neutron spectrum in the PWR. We can obtain the following equation by a change in variable $u = \ln(E_0/E_n)$, which provides a new integration boundary, which is approximated as 23.03 0.

$$\sigma_{x,r} = \int_0^{23.03} du\sigma_{x,r}(u)[E_n\chi(E_n)](u), \tag{12}$$

where E_0 = 10 MeV, u is often referred to as lethargy, and $\phi = E_n\chi(E_n)$ is referred to as the normalized neutron spectrum.

3 Results and discussion

3.1 Determination of Gaussian parameters

The fitting results of ^{233,235,238}U(n,f) and ^{239,240,241}Pu(n,f) are shown with experimental data from [45–55] in Figs. 3 and 4.

We applied the curve fitting results using the least squares method and obtained the parameters of the Gaussian functions in Eq. (1), which can be used in the study of neutron-induced fission within the excitation energy range of the thermal energy of up to 10 MeV. The parameter Y_3 increases exponentially with increasing excitation energy, which results in an increase in the peak-to-valley ratio directly. Under the premise that $\frac{A_F}{2} - nt$ is the symmetric axis in the mass distribution, Δ_3 is fixed at 0. Δ_i and σ_i are assumed to be constant for a fixed fission system. In addition, $2nt$ denotes the total number of neutrons emitted, which increases slightly with an increase in the excitation energy.

For uranium, Δ_i and σ_i exhibit a linear relationship with the mass number of a compound nuclei. The Gaussian parameters are expressed as a function of the mass number and excitation energy. The parameters in Eq. (1) can be expressed as follows:

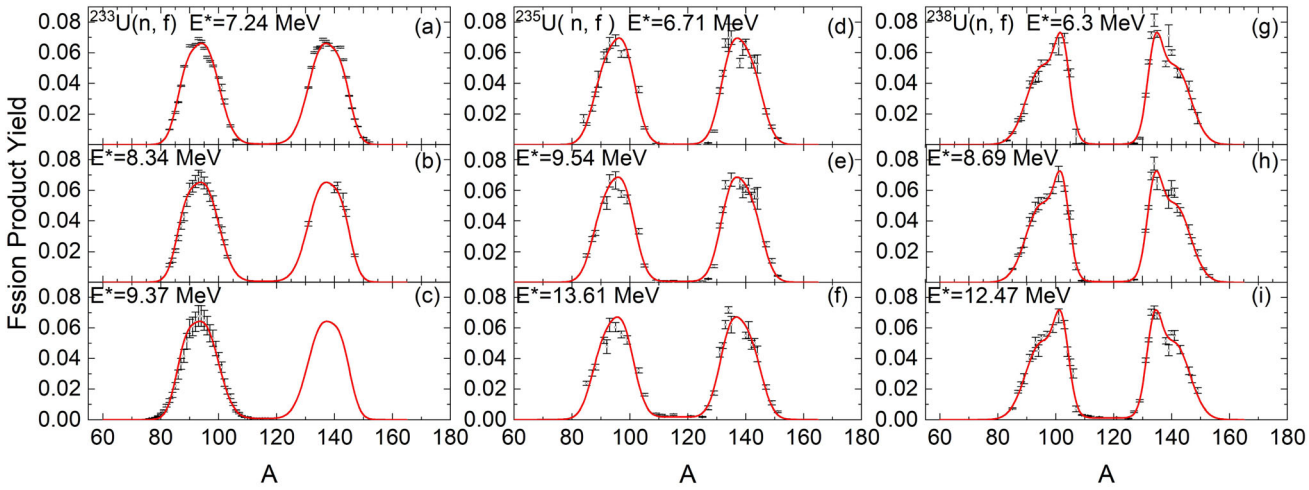

Fig. 3 (Color online) Fitting results for ^{233}U(n,f), ^{235}U(n,f), and ^{238}U(n,f). The lines represent the curve-fitting results. Black dots with error bars denote the experimental data [52–55]

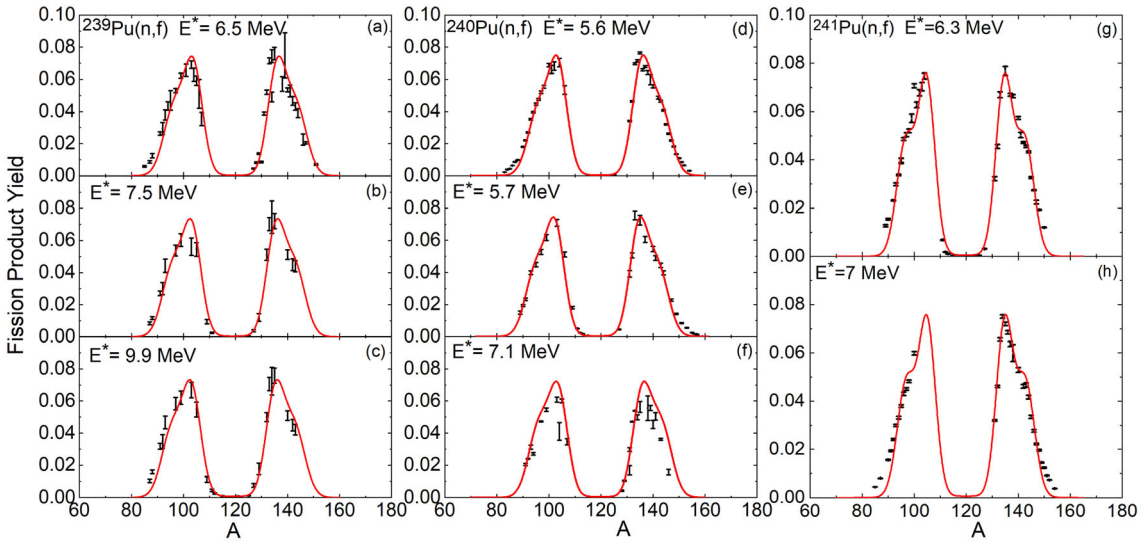

Fig. 4 (Color online) Fitting results for ^{239}Pu(n,f), ^{240}Pu(n,f) and ^{241}Pu(n,f). The lines represent the curve-fitting results. Black dots with error bars denote the experimental data [45–51]

$$\begin{cases} \sigma_i = par1(A_{\mathrm{F}} - 1) + par2, \\ \Delta_i = par1(A_{\mathrm{F}} - 1) + par2, \\ nt = \big(par1(A_{\mathrm{F}} - 1) + par2\big)E^* + par3, \\ Y_3 = \exp\{(par1(A_{\mathrm{F}} - 1) + par2)E^* \\ \quad +(par3(A_{\mathrm{F}} - 1) + par4)\}, \\ Y_2 = Y_3\{(V_{\mathrm{mid}} - V_{\mathrm{min}})/(0.055(A_{\mathrm{F}} - 1) - 9.215)\}^{5.7}, \\ Y_1 = 1 - Y_2 - \dfrac{Y_3}{2}, \end{cases} \tag{13}$$

where $par1$, $par2$, $par3$, and $par4$ are listed in Table 1. In addition, V_{mid} and V_{min} denote the values of potential energy with a symmetry configuration and combinations with proton and neutron shell closures, respectively, as shown in Fig. 2. Moreover, E^* is the excitation energy of the fission system.

For the case of plutonium isotopes, because the mass numbers of ^{239}Pu, ^{240}Pu, and ^{241}Pu are close to each other, the dependence of the Gaussian parameters on the mass number is not obvious. An assumption of the mass number correlation is not made for the Gaussian parameters. In addition, $\frac{Y_2}{Y_3}$ can be obtained using the following expression:

$$\frac{Y_2}{Y_3}=\left(\frac{V_{\mathrm{mid}}-V_{\mathrm{min}}}{2.9}\right)^{7.5}. \quad (14)$$

The value of Y_i depends on the excitation energy. The parameters σ_i and Δ_i were chosen to be fixed by changing the excitation energy. The values of the Gaussian parameters for ^{239}Pu, ^{240}Pu, and ^{241}Pu are listed in Table 2.

Table 2 Fixed Gaussian parameters (σ_4, σ_5, Δ_4, and Δ_5 are assumed to satisfy the conditions $\sigma_4=\sigma_2$, $\sigma_5=\sigma_1$, $\Delta_1+\Delta_5=0$, and $\Delta_2+\Delta_4=0$)

Nuclide	σ_1	σ_2	σ_3	Δ_1	Δ_2
^{239}Pu	4	3.5	17.5	23.5	16
^{240}Pu	4	3.5	17.5	23.5	16
^{241}Pu	3.5	3.2	17.5	22.9	14.9

3.2 Comparisons with experimental data

Owing to the scarce independent yield data of the fission products, we fit the data to the cumulative yields to investigate the energy dependence. In Figs. 5 and 6, the calculated isotope yields from the fitted mass distributions of ^{235}U(n_{th},f) and ^{239}Pu(n_{th},f) were compared with the experimental data [56–59]. Numerical comparisons of the experimental independent and simulated yields for ^{235}U(n_{th},f) and ^{239}Pu(n_{th},f) are shown in Tables 3 and 4. As shown in Tables 3 and 4, we present the errors in the experimental fragments and compare the simulation results with the experimental data. Within the permissible range of errors, the thermal neutron-induced fission yields predicted by our simulations are in good agreement with the experimental data, which proves the validity of our methods and models.

To further verify the feasibility of our method in the establishment of fission product charge distribution, we compared the calculated charge distribution and experimental data in the reactions ^{235}U(n_{th},f) and ^{239}Pu(n_{th},f), as shown in Fig. 7). The experimental data were obtained from [59]. The calculated peak is slightly higher than the experimental data. However, both the calculated yield and experimental data reached the maximum at approximately $Z = 54$, which might suggest a transition of shell closure from $Z = 50$ to $Z = 54$.

3.3 Neutron spectrum

Based on the Daya Bay nuclear power plant, a neutron spectrum was established by modeling an actual reactor core using MCNP4C [60]. The neutron spectrum in the nuclear reactor generally ranges from 0.001 eV to 10 MeV and is separated into three parts: thermal neutron energy, epithermal (intermediate) neutron energy, and fast neutron energy. Thermal neutron energy ranges from 0.001 to 0.1 eV, where most fission reactions take place in a PWR. The fast neutron energy ranges from 10^5 eV to 10 MeV. Most of these neutrons are emitted before and after fission. The energy of epithermal neutrons is between 0.1 and 10^5 eV. In thermal neutron reactors, neutrons emitted during the fission process have an average energy of 2 MeV. The neutrons lose energy by elastic or inelastic collisions with nuclei in the moderator medium until they become thermal neutrons. Most fission reactions in thermal nuclear reactors are induced through thermal neutrons.

The neutron spectrum is often referred to as

$$\phi = E_{\mathrm{n}} \times \chi(E_{\mathrm{n}}), \quad (15)$$

where ϕ is the neutron spectrum, $\chi(E_{\mathrm{n}})$ is the neutron distribution probability density at an energy of E_{n}.

A piecewise function was used to describe the neutron spectrum. In the thermal neutron region, $\chi(E_{\mathrm{n}})$ is often approximated using a Maxwellian–Boltzmann distribution. A method of superposing five to seven partial Maxwellian distributions to represent the neutron spectrum within the thermal and epithermal range was proposed in [25]. We found that a single Maxwellian distribution is sufficient to

Table 1 Values of *par*1, *par*2, *par*3, and *par*4 for different parameters

Parameters	*par*1	*par*2	*par*3	*par*4
σ_1	0.421 ± 0.017	− 94.818 ± 4.039		
σ_2	− 0.482 ± 0.041	117.18 ± 9.57		
σ_3	0	20		
Δ_1	− 0.866 ± 0.050	229.12 ± 11.80		
Δ_2	− 0.895 ± 0.046	228.89 ± 10.73		
nt	− 0.0033 ± 0.0002	0.837 ± 0.043	0.957 ± 0.004	
$Y_3(A_{\mathrm{F}} \le 236)$	− 0.00805 ± 0.00001	2.155 ± 0.002	− 0.1106 ± 0.0001	20.05 ± 0.03
$Y_3(A_{\mathrm{F}} > 236)$	− 0.00250 ± 0.00001	0.851 ± 0.002	− 0.0146 ± 0.0003	− 2.50 ± 0.05

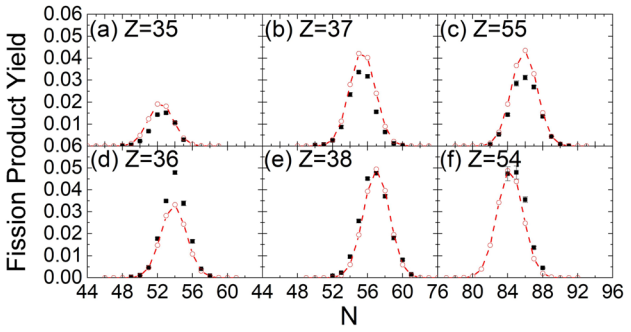

Fig. 5 (Color online) Normalized isotope yields of fission fragments in $^{235}U(n_{th},f)$ are compared with the experimental data. The hollow points are the calculated results. The red dashed lines are the guidelines. The black solid points represent the experimental data. Data for light fragments were taken from [56]. Data for fragments with $Z = 54$ and $Z = 55$ were obtained from [57] and [58]

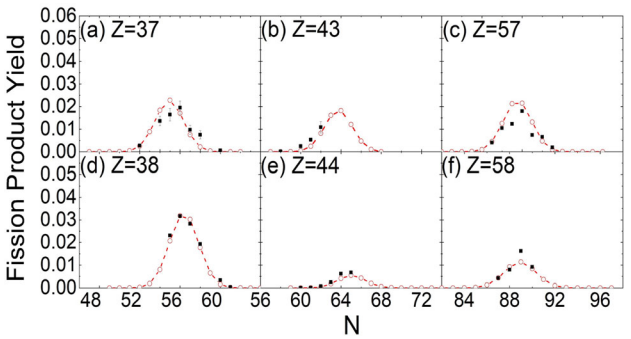

Fig. 6 Normalized isotope yields of fission fragments in $^{239}Pu(n_{th},f)$ are compared with the experimental data. The hollow points are the calculated results. The red dashed lines are the guidelines. The black solid points represent the experimental data. Experimental data were obtained from [59]

describe the neutron spectrum within the thermal range. The multi-Maxwellian distribution mainly takes effect in the transition part between the thermal and epithermal ranges. The formula used is as follows:

$$\chi(E_n) = \alpha_M^2 \exp(-E_n\alpha_M)E_n, \tag{16}$$

where α_M is related to the temperature of the moderating medium [25]:

$$\alpha_M = \frac{1}{T_m}. \tag{17}$$

Here, T_m is the temperature of the moderating medium.

The experimental thermal neutron energy distribution in the case of a water-moderated reactor was compared in [61]. Figure 8 shows a comparison of the experimental thermal neutron spectrum in water moderated reactors at 291.15 and 371.15 K with the calculation results in this study. It can be seen that the calculated results can reproduce the experimental data quite well.

Within the epithermal neutron energy range, the probability density of the neutron energy distribution follows the $\frac{1}{E_n}$ law. To make the transition smoother between the three different regions and more suitable to the results in [60], the probability density in this region is assumed as

$$\chi(E_n) = C\frac{1}{(E_n)^{0.9}} + \frac{0.02}{(E_n)^{2.1}} + \frac{7}{10^7 - E_n}, \tag{18}$$

where C is a constant determined by the continuous condition at the boundary of the thermal and epithermal energy ranges.

In the fast neutron energy range of the PWR, $\chi(E_n)$ is approximated by the thermal neutron-induced fission spectrum of ^{235}U. The experimental data and curve fitting results of the ^{235}U fission spectrum are presented in [62, 63]. In [63], the prompt neutron spectrum from thermal neutron-induced fission in ^{235}U using the recoil proton method was recently measured. In [62], a photographic plate method and time-of-flight method are employed. Two different formulas are used in curve fitting, all of which fit well with the experimental data. In this study, the fission spectrum of ^{235}U is considered as a linear combination of the two formulas and can be written as

$$\chi(E_n) = C_1(\omega\sqrt{E_n}e^{-E_n/E_M} + (1-\omega)e^{-E_n/a}\sinh\sqrt{bE_n}), \tag{19}$$

where ω denotes the weight, and E_M, a, and b are constants. These were all determined in [64] using the least-squares method. In addition, C_1 is determined based on the continuous condition at the boundary of the epithermal and fast energy ranges. The normalized neutron spectrum within all energy ranges was multiplied by a normalized constant C_{norm}.

In this study, the boundaries between the three energy ranges were $10^{-0.6}$ and $10^{5.7}$ eV. In addition, T_m is taken as 563.15 K. In Fig. 9, the normalized neutron spectrum in the PWR was compared with the calculated results obtained in [60]. In our mathematical description of the neutron spectrum, the resonance in the epithermal energy range was not considered.

3.4 Effective cross section in PWR

In Table 5, we list the effective fission and neutron capture cross-sections of several heavy nuclides calculated using Eq. (11). The cross-section data are taken from the ENDF library, and the neutron spectrum proposed above (Eqs. (16), (18), and (19)) are used to calculate the effective cross sections.

The calculated results were compared with the effective cross sections from [43]. The cross sections from the

Table 3 Comparison of experimental independent yield data and simulated yield data for $^{235}U(n_{th},f)$

Nuclide	Experimental yield	Simulated yield	Relative difference
^{83}Br	0.00020 ± 0.00004	0.00016	− 0.210
^{84}Br	0.00048 ± 0.00007	0.00111	1.313
^{85}Br	0.00224 ± 0.00009	0.00480	1.143
^{86}Br	0.00674 ± 0.00024	0.01237	0.835
^{88}Br	0.01428 ± 0.00026	0.01911	0.338
^{89}Br	0.01512 ± 0.00052	0.01814	0.200
^{90}Br	0.01067 ± 0.00044	0.01029	− 0.036
^{91}Br	0.00287 ± 0.00021	0.00359	0.251
^{85}Kr	0.00039 ± 0.00007	0.00010	− 0.744
^{86}Kr	0.00113 ± 0.00009	0.00087	− 0.228
^{87}Kr	0.00468 ± 0.00024	0.00456	− 0.026
^{88}Kr	0.01769 ± 0.00054	0.01465	− 0.172
^{89}Kr	0.03489 ± 0.00042	0.02814	− 0.193
^{90}Kr	0.04782 ± 0.00070	0.03320	− 0.306
^{91}Kr	0.03384 ± 0.00107	0.02427	− 0.283
^{92}Kr	0.01644 ± 0.00077	0.01082	− 0.342
^{93}Kr	0.00402 ± 0.00022	0.00305	− 0.241
^{94}Kr	0.00092 ± 0.00019	0.00054	− 0.414
^{87}Rb	0.00041 ± 0.00012	0.00004	− 0.903
^{88}Rb	0.00069 ± 0.00014	0.00043	− 0.371
^{89}Rb	0.00252 ± 0.00034	0.00282	0.119
^{90}Rb	0.00860 ± 0.00065	0.01127	0.310
^{91}Rb	0.02347 ± 0.00092	0.02789	0.188
^{92}Rb	0.03354 ± 0.00045	0.04208	0.255
^{93}Rb	0.03167 ± 0.00079	0.04021	0.270
^{94}Rb	0.01557 ± 0.00051	0.02402	0.543
^{95}Rb	0.00636 ± 0.00024	0.00893	0.404
^{96}Rb	0.00115 ± 0.00020	0.00211	0.835
^{97}Rb	0.00037 ± 0.00018	0.00031	− 0.170
^{90}Sr	0.00081 ± 0.00024	0.00014	− 0.827
^{91}Sr	0.00229 ± 0.00027	0.00118	− 0.485
^{92}Sr	0.00959 ± 0.00067	0.00600	− 0.374
^{93}Sr	0.02571 ± 0.00084	0.01942	− 0.245
^{94}Sr	0.04506 ± 0.00052	0.03928	− 0.128
^{95}Sr	0.04756 ± 0.00056	0.04940	0.039
^{96}Sr	0.03701 ± 0.00075	0.03958	0.069
^{97}Sr	0.01794 ± 0.00074	0.01949	0.086
^{98}Sr	0.00818 ± 0.00046	0.00593	− 0.275
^{99}Sr	0.00155 ± 0.00022	0.00112	− 0.277
^{138}Xe	0.0473 ± 0.0032	0.04865	0.029
^{139}Xe	0.048 ± 0.003	0.04381	− 0.085
^{140}Xe	0.0355 ± 0.0013	0.02477	− 0.302
^{141}Xe	0.01360 ± 0.00060	0.00868	− 0.362
^{142}Xe	0.00447 ± 0.00020	0.00194	− 0.566
^{137}Cs	0.00061 ± 0.00006	0.00130	1.145
^{138}Cs	0.00532 ± 0.00021	0.00627	0.179
^{139}Cs	0.01430 ± 0.00055	0.01912	0.337

Table 3 continued

Nuclide	Experimental yield	Simulated yield	Relative difference
^{140}Cs	0.0284 ± 0.0012	0.03661	0.289
^{141}Cs	0.031 ± 0.001	0.04345	0.397
^{142}Cs	0.02684 ± 0.00072	0.03280	0.222
^{143}Cs	0.01355 ± 0.00037	0.01521	0.123
^{144}Cs	0.00428 ± 0.00010	0.00434	0.014
^{145}Cs	0.00085 ± 0.00003	0.00077	− 0.101
^{146}Cs	0.000076 ± 0.000006	0.00009	0.070

Table 4 Comparison of experimental independent yield data and simulated yield data for ^{239}Pu(n_{th},f)

Nuclide	Experimental yield	Simulated yield	Relative difference
^{89}Rb	0.00271 ± 0.00088	0.00249	− 0.081
^{91}Rb	0.0136 ± 0.0021	0.01834	0.349
^{92}Rb	0.0164 ± 0.0028	0.02279	0.390
^{93}Rb	0.0195 ± 0.0030	0.01707	− 0.125
^{94}Rb	0.0097 ± 0.0020	0.00759	− 0.218
^{95}Rb	0.0075 ± 0.0018	0.00209	− 0.721
^{97}Rb	0.00057 ± 0.00089	0.000038	− 0.934
^{93}Sr	0.02310 ± 0.00025	0.02076	− 0.101
^{94}Sr	0.03168 ± 0.00034	0.0318	− 0.004
^{95}Sr	0.02820 ± 0.00031	0.03024	0.072
^{96}Sr	0.01927 ± 0.00021	0.01771	− 0.081
^{98}Sr	0.00331 ± 0.00013	0.00152	− 0.541
^{99}Sr	0.000400 ± 0.000004	0.00022	− 0.445
^{101}Tc	0.00014 ± 0.00009	0.000003	− 0.980
^{103}Tc	0.00241 ± 0.00097	0.00043	− 0.821
^{104}Tc	0.00536 ± 0.00083	0.00247	− 0.539
^{105}Tc	0.01086 ± 0.00251	0.00818	− 0.247
^{104}Ru	0.00004 ± 0.00001	0.000006	− 0.852
^{105}Ru	0.00008 ± 0.00001	0.00007	− 0.154
^{106}Ru	0.00007 ± 0.00003	0.00046	− 0.363
^{107}Ru	0.00253 ± 0.00028	0.00179	− 0.292
^{108}Ru	0.00619 ± 0.00025	0.00409	− 0.339
^{109}Ru	0.00674 ± 0.00046	0.00549	− 0.185
^{142}La	0.00406 ± 0.00006	0.00447	0.101
^{143}La	0.01045 ± 0.00016	0.01253	0.199
^{144}La	0.01228 ± 0.00024	0.02129	0.734
^{145}La	0.01796 ± 0.00027	0.02148	0.196
^{146}La	0.00742 ± 0.00010	0.01315	0.772
^{147}La	0.00655 ± 0.00011	0.00472	− 0.279
^{148}La	0.00191 ± 0.00003	0.00101	− 0.471
^{145}Ce	0.00430 ± 0.00008	0.00437	0.016
^{146}Ce	0.00793 ± 0.00019	0.00922	0.163
^{147}Ce	0.01619 ± 0.00031	0.01141	− 0.295
^{148}Ce	0.00920 ± 0.00022	0.00838	− 0.089

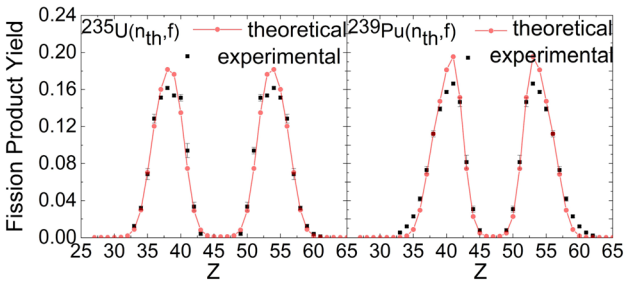

Fig. 7 (Color online) Normalized charge distribution of the fission fragments in $^{235}U(n_{th},f)$ and $^{239}Pu(n_{th},f)$ are compared with the experimental data. Red dots are the calculated results, and red lines are the guidelines. The black solid points are the experimental data taken from [59]

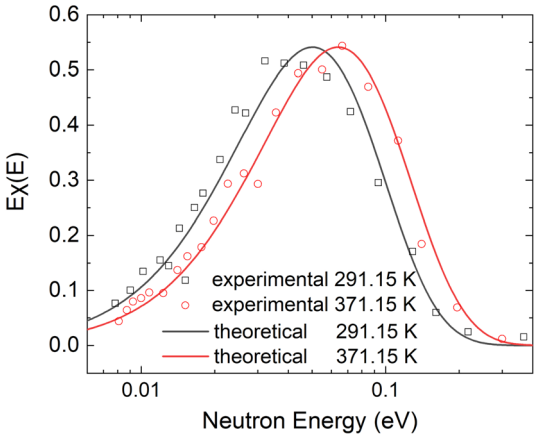

Fig. 8 (Color online) Comparison of the thermal neutron spectrum in the case of a water moderated reactor at 291.15 and 371.15 K. Hollow points are the experimental data [61]. Lines represent the theoretical results calculated in this study

ENDF reflect the resonance absorption of neutrons around the epithermal energy range. However, for some nuclei such as ^{238}U, the resonance phenomenon of the reaction cross sections leads to a deviation during the integration process in Eq. (12). However, in [43], the differential cross sections are continuous without showing the resonance phenomenon, which makes the integration results more precise. Because $^{238}U(n, \gamma)$ plays an important role in the uranium-plutonium cycle, we use the fission-to-capture ratio in [43] to calibrate the capture cross section of ^{238}U.

3.5 Operational parameters of nuclear power plant

The characteristics of the Daya Bay nuclear power plant were adopted [65], and some characteristics are listed in Table 6. It is assumed that the reactor operates at a full power of 330 days per year. The energy production is assumed to be constant. In this study, the initial enrichment is assumed to be 3%, and the fuel cycle performance with ^{235}U enrichments of above 5% was studied in [66]. The

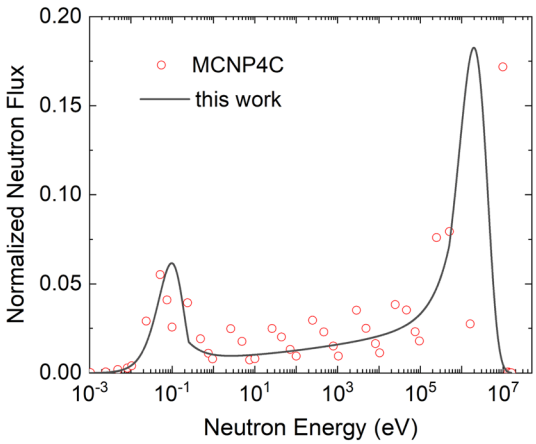

Fig. 9 The neutron spectrum established in this study is compared with the results simulated by MCNP4C in [60]. The solid line represents the neutron spectrum in this study. Dots refer to the calculations [60]

moderator temperature was assumed to be 290°C. The neutron flux was determined using the following equation:

$$P = \sum\nolimits_{\mathrm{f}} \Phi V E_{\mathrm{f}}, \tag{20}$$

where P is the thermal power of the reactor, $\sum_{\mathrm{f}}$ denotes the macroscopic fission cross section, Φ is the neutron flux, and E_{f} represents the energy released in one fission event of ^{235}U. In addition, V is the volume of the reactor core. In this study, it is considered that the energy released in one fission event of ^{235}U is 200 MeV. In general, decreasing the fission cross section leads to an increase in the neutron flux as the fuel consumption increases.

3.6 Long-lived heavy nuclides in PWR

In this section, the inventory of long-lived heavy nuclides as a function of fuel consumption is studied. The fuel consumption was calculated using the following equation:

Table 5 Effective fission (σ_{f}) and neutron capture (σ_{c}) cross sections for several heavy nuclides

Nuclide	σ_{f} (barns)	σ_{c} (barns)	$\sigma_{\mathrm{f}}/\sigma_{\mathrm{c}}$	$\sigma_{\mathrm{f}}/\sigma_{\mathrm{c}}$ in Ref. [43]
^{242}Cm	1.2005	3.0541	0.3931	0.2653
^{241}Am	0.9706	89.5744	0.0108	0.0129
^{241}Pu	102.3696	35.9113	2.8506	2.9619
^{239}Pu	89.4405	45.7218	1.9562	1.7977
^{237}Np	0.5362	22.5075	0.0238	0.0153
^{238}U	0.1171	3.2031	0.0366	0.1195
^{235}U	44.6759	8.8204	5.0651	4.2982

$$B_{\mathrm{U}} = \frac{\int_0^T P(t)\mathrm{d}t}{M_{\mathrm{U}}}, \tag{21}$$

where B_{U} is the uranium burnup, P represents the thermal power as a function of time, T indicates the total operation time of the reactor. According to [67], a reactor in Daya Bay nuclear plant goes through a shutdown and refueling process every 1 and a half years. Each refueling process lasted for approximately 40 days. In addition, the reactor operates normally at full power on other days. Therefore, for actual fuel utilized for a 1-year period and fuel burned incessantly under full power for approximately 330 days, it is assumed in this study that the burnup in both cases is equivalent. As a result, for a time scale of 1 year, the numerator of Eq. (21) can be expressed as the maximum and constant thermal power multiplied by 330 days. In addition, M_{U} indicates the total mass of uranium in the fuel.

Figure 10 illustrates the evolution of inventories of uranium isotopes with burnup. It is noted that for the isotopes of uranium, the inventory of ^{238}U remains essentially constant. Here, (n, γ) is the primary consumption path of ^{238}U owing to the small effective microscopic fission cross sections. With a gradual decrease in the slope, the value of ^{235}U starts to stabilize at deep burnup after 180 GW·d/t. Compared to the inventory of ^{235}U, ^{234}U, and ^{236}U are insignificant under a low fuel consumption before reaching 50 GW·d/t. However, the inventory of ^{236}U exceeds that of ^{235}U after the burnup at approximately 50 GW·d/t. The inventory of ^{234}U is higher than that of ^{235}U at a deeper burnup. The inventory of ^{233}U is maintained at an extremely low level after reaching a steady state.

Partitioned from the PWR, plutonium can be reutilized in the fuel transition to the thorium fuel cycle in a thermal molten salt reactor [68]. The variation in plutonium isotope inventories with burnup is shown in Fig. 11. It is observed that the inventory of ^{239}Pu is higher than that of several isotopes. The significant generation of ^{239}Pu at low burnup is the result of a large amount of neutron capture by ^{238}U and the relatively short half-lives of β-decay of ^{239}U and ^{239}Np. In addition, the ^{240}Pu and ^{241}Pu levels were maintained at essentially the same level after stabilization. The inventory of ^{242}Pu increases with the burnup and approaches that of ^{239}Pu. In Ref. [28], the calculated results in a thermal molten salt reactor using Th-U mixed fuel reflect the same relative inventory of ^{242}Pu. The main source of ^{242}Pu is the orbital electron capture of ^{242}Am. Its relatively short half-life results in a significant inventory of ^{242}Pu at a deeper burnup.

In Fig. 12, the inventories of neptunium isotopes are presented. It can be seen that both ^{237}Np and ^{238}Np stabilized after burnup at approximately 80 GW·d/t. The inventories of the americium and curium isotopes are presented in Figs. 13 and 14. The inventories of the light isotopes are relatively high for both americium and curium isotopes. The heavier isotopes are essentially produced by the neutron capture reaction of lighter isotopes. In addition, some isotopes tend to have the same value at a deeper burnup. The inventory of ^{243}Am was close to that of ^{242}Am. The same phenomenon was observed for pairs of (^{243}Cm, ^{244}Cm) and (^{245}Cm, ^{246}Cm). This can be explained by comparing the microscopic fission cross sections shown in Table 7. For nuclei such as ^{244}Cm, ^{246}Cm, and ^{243}Am, their fission cross sections are much smaller than those of other isotopes, which leads to less consumption and gradual accumulation.

Figure 15 presents the variation of inventories of uranium and plutonium isotopes with the burnup. It can be seen that the calculated results of the relative inventories and the variation trend in our model are in surprisingly good agreement with the experimental data from Daya Bay. Further investigation is therefore justified, although the calculated absolute inventory of each isotope is higher than the experimental value because the enrichment of uranium used in our simulations was higher than the fuel used in [69], whereas the assumed neutron flux of the reactor is kept at a relatively high level.

The total macroscopic fission cross sections and the principal contribution of fission cross sections of fissile nuclides are presented in Fig. 16. It was observed that the

Table 6 Operating parameters of Daya Bay nuclear power plant

Parameters	Designed value	Actual value
Maximum continuous electrical power (MW)	984	984
Rated thermal power (MW)	2905	2905
Thermal efficiency (%)	33.87	34.1
Initial enrichment (%)	1.8/2.4/3.1	1.8/2.4/3.1
Initial total inventory of uranium (t)	72.14	72.14
Fuel assembly model	AFA-2G	AFA-2G
Coolant inlet temperature (°C)	292.4	293.5
Coolant outlet temperature (°C)	327.6	326.5

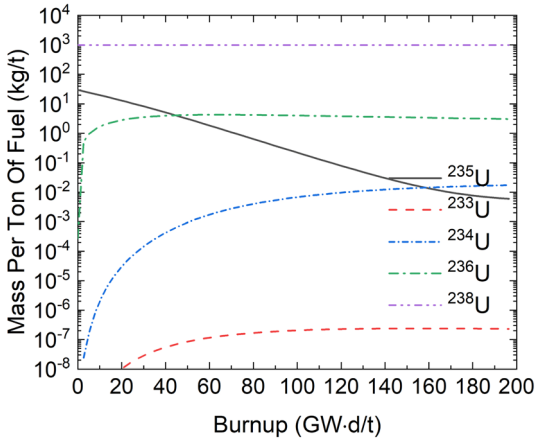

Fig. 10 (Color online) Calculated inventories of uranium isotopes in PWR as a function of burnup

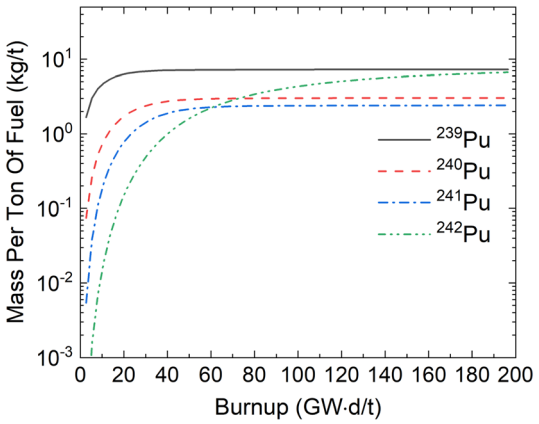

Fig. 11 (Color online) Calculated inventories of plutonium isotopes in a PWR as a function of burnup

total fission cross section continued to decrease during the reactor operation. At a lower burnup, it decreases with a slower rate of change, which is mainly caused by a rapid consumption of ^{235}U, alleviated by the growth of ^{239}Pu and ^{241}Pu. With the stabilization of the ^{239}Pu and ^{241}Pu inventory, the sustained decrease of ^{235}U leads to a decrease in the total macroscopic fission cross sections.

Typically, PWR nuclear power plants have a discharge burnup of over 45 GW·d/t. Table 8 shows the predictions of the inventory of heavy long-lived nuclides at 50 GW·d/t and 196 GW·d/t under full-power operation.

3.7 Fission fragments in a PWR

As shown in Table 9, we simulated the nuclide inventory on three decay chains. According to the data provided in [70], the relative inventories of long-lived nuclides are reasonable. Figure 17 presents the evolution of several long-lived nuclides in a PWR under 100% power. As can be observed in Fig. 17, long-lived nuclides increase linearly during the evolution. This accumulation is due to the long half-lives. A few long-lived nuclides can be consumed within a fuel cycle.

On the one hand, Table 9 indicates that the short-lived nuclides are maintained at an extremely low level. For example, the inventory of ^{135}Sn is approximately 10^{-13} kg/t. On the other hand, the long-lived nuclide ^{135}Cs is greater than the others, and during a 600-day period, increases linearly. For the isobars of ^{135}Cs, it can be seen that their concentration does not increase significantly because of their short half-life; they increase slowly and start to stabilize at a deeper burnup. Specifically, the inventories of ^{135}Xe and ^{135}I are all 10^{-4} kg/t at 20 GW·d/t.

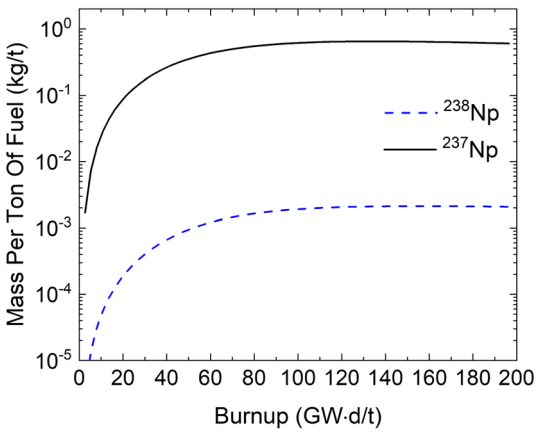

Fig. 12 (Color online) Calculated inventories of neptunium isotopes in a PWR as a function of burnup

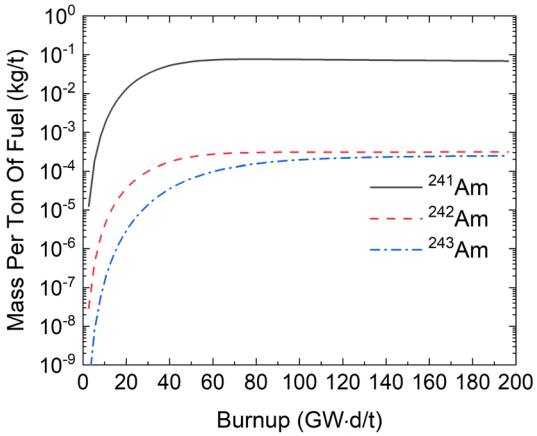

Fig. 13 (Color online) Calculated inventories of americium isotopes in a PWR as a function of burnup

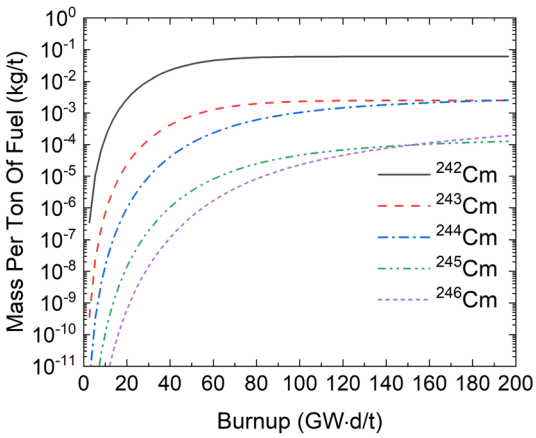

Fig. 14 (Color online) Calculated inventories of curium isotopes in a PWR as a function of burnup

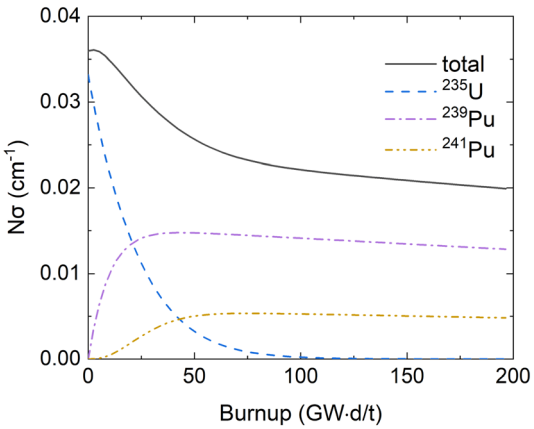

Fig. 16 Calculated total macroscopic fission cross sections and the principle components of fission cross sections

Table 7 Effective fission (σ_f) and neutron capture (σ_c) cross sections for Cm and Am isotopes

Nuclide	σ_f (barns)	σ_c (barns)
^{246}Cm	0.5213	1.369
^{245}Cm	129.5611	20.7079
^{244}Cm	0.832	7.6435
^{243}Cm	62.0526	11.2636
^{243}Am	0.4443	27.3167
^{242}Am	200.1696	21.5212

4 Summary

As an important aspect of the study on the fission mode and fission fragment inventories in nuclear reactors, fragment yields of fissile nuclides have been investigated for decades. The five Gaussian functions and the most probable charge model were combined to investigate the fission yields in a PWR. The potential energy surface based on the di-nuclear system concept was applied to evaluate the physical properties of the fission process. In addition, the neutron incident energy effects on the fission product distribution are considered.

The neutron spectrum in a PWR under stabilization was established using a piecewise function. The inventories of long-lived heavy nuclei and fission fragments in the PWR were predicted by solving a set of differential equations coupled to multiple variables. In this study, mathematical expressions for the neutron energy spectrum in a PWR were established, and effective microscopic cross sections were calculated using data from the ENDF library. The operating parameters of the Daya Bay nuclear power station were used to simulate the inventories of heavy nuclei and fission fragments. For the heavy nuclei, the evolution

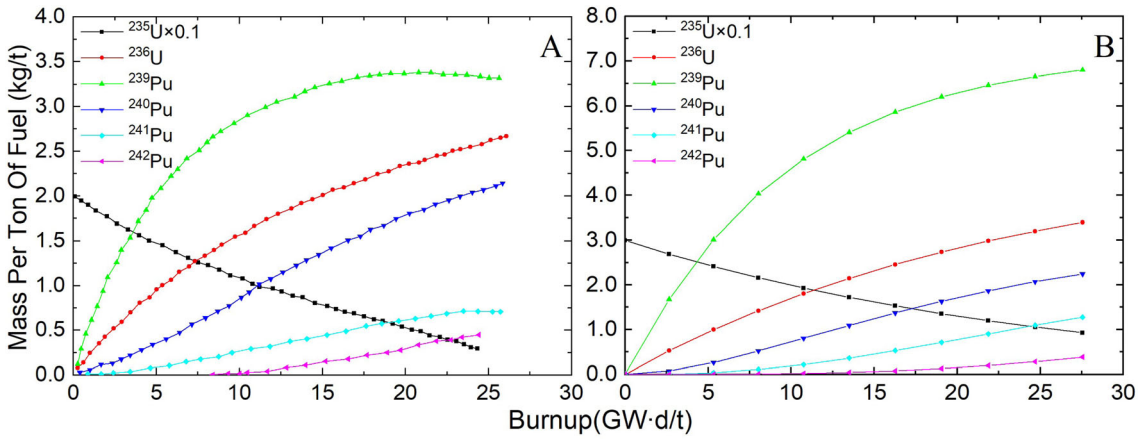

Fig. 15 (Color online) Comparison of heavy nuclide inventories between (A) experimental data [69] and (B) calculated results in a PWR

Table 8 Prediction of heavy long-lived nuclides in a PWR

Nuclide	Half-life (year)	Inventory (kg/t)	
		50 GW·d/t	196 GW·d/t
^{246}Cm	4723	6.13×10^{-7}	1.92×10^{-4}
^{245}Cm	8250	3.85×10^{-6}	1.28×10^{-4}
^{244}Cm	18.11	1.24×10^{-4}	0.0026
^{243}Cm	28.9	8.73×10^{-4}	0.0025
^{242}Cm	0.4459	0.036	0.060
^{243}Am	7367	6.81×10^{-5}	2.46×10^{-4}
^{241}Am	432.6	0.068	0.069
^{242}Pu	3.73×10^{5}	1.67	6.67
^{241}Pu	14.33	2.17	2.41
^{240}Pu	6561	2.90	3.03
^{239}Pu	2.41×10^{4}	7.17	7.28
^{237}Np	2.14×10^{6}	0.36	0.60
^{238}U	4.47×10^{9}	978.77	976.81
^{236}U	2.34×10^{7}	4.21	3.06
^{235}U	7.04×10^{8}	2.94	0.0060
^{234}U	2.46×10^{5}	0.001	0.017
^{233}U	1.59×10^{5}	8.78×10^{-8}	2.30×10^{-7}
^{231}Pa	3.27×10^{4}	4.10×10^{-13}	7.17×10^{-15}
^{232}Th	1.40×10^{10}	2.96×10^{-7}	1.14×10^{-6}
^{227}Ac	21.772	4.03×10^{-13}	7.05×10^{-15}
^{226}Ra	1600	6.26×10^{-19}	2.75×10^{-18}

Table 9 Prediction of fission products in a PWR

Nuclide	Half-life (year)	Inventory (kg/t) 20 GW·d/t
^{90}Br	6.09×10^{-8}	1.29×10^{-9}
^{90}Kr	1.02×10^{-6}	1.94×10^{-7}
^{90}Rb	5.01×10^{-6}	1.32×10^{-6}
^{90}Sr	28.90	3.18×10^{-1}
^{107}Mo	1.10×10^{-7}	2.00×10^{-9}
^{107}Tc	6.72×10^{-7}	7.47×10^{-8}
^{107}Ru	7.13×10^{-6}	1.05×10^{-6}
^{107}Rh	4.12×10^{-5}	6.12×10^{-6}
^{107}Pd	6.50×10^{6}	1.16×10^{-1}
^{135}Sn	1.68×10^{-8}	8.88×10^{-13}
^{135}Sb	5.32×10^{-8}	7.18×10^{-10}
^{135}Te	6.02×10^{-7}	1.67×10^{-7}
^{137}Te	7.89×10^{-8}	2.32×10^{-9}
^{135}I	7.50×10^{-4}	5.89×10^{-4}
^{137}I	7.77×10^{-7}	3.27×10^{-7}
^{135}Xe	1.04×10^{-3}	8.60×10^{-4}
^{137}Xe	7.26×10^{-6}	5.86×10^{-6}
^{135}Cs	2.30×10^{6}	8.47×10^{-1}
^{137}Cs	30.08	8.56×10^{-1}

of uranium, plutonium, neptunium, americium, and curium isotopes were investigated. The inventories of ^{234}U and ^{236}U exceed that of ^{235}U after reaching a discharge burnup. Among the plutonium isotopes, the inventory of ^{242}Pu increases and gradually reaches the same level as ^{239}Pu under a deep burnup. Because of the single decay chain for americium and curium isotopes and their large difference in effective fission cross sections, the inventories of the isotopes decrease with an increase in mass number. By contrast, isotope pairs such as ^{243}Am and ^{242}Am tend to have similar inventories after stabilization. Upon discharge burnup, except for ^{238}U, the inventories of ^{239}Pu, ^{240}Pu, ^{241}Pu, ^{242}Pu, ^{237}Np, ^{235}U, and ^{236}U are predominant in a PWR. For fission fragments, the evolution of several long-lived fission fragments is predicted, and inventories of isobars of ^{135}Xe were calculated. We also compared the calculated inventories of uranium and plutonium isotopes with experimental data from Daya Bay. Surprisingly, the evolution trends and relative values were in good agreement with the data. In the future, our group will optimize the calculation of the reaction cross sections and consider more conversions between nuclides, allowing the method to be improved and better predict the inventories of long-lived isotopes.

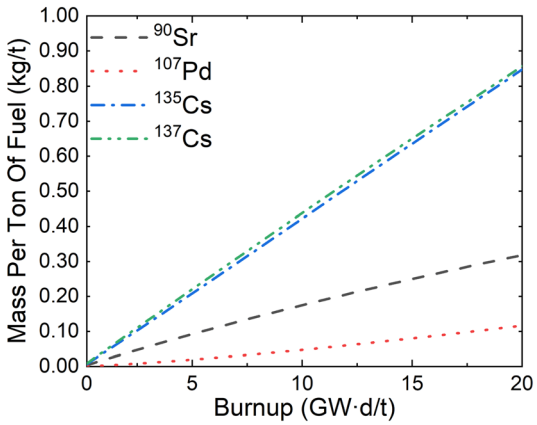

Fig. 17 (Color online) Evolution of long-lived nuclides during a fuel cycle

Acknowledgements The authors thank Dr. Li-Le Liu and Chao-Sheng Zhou for their useful discussions.

Author contributions All authors contributed to the study conception and design. Material preparation, data collection, and analysis were performed by Ze-Xin Fang, Meng Yu, and Long Zhu. The first draft of the manuscript was written by Ze-Xin Fang and Meng Yu. All authors commented on previous versions of the manuscript. All authors read and approved the final manuscript.

References

1. C.H. Zeng, ^{235}U Fission product radiological calculations in nuclear fuel reactors. China J. Nuclear Sci. Eng. **12**, 81–86 (1992). **(in Chinese)**
2. Z.L. Xu, X.C. Wu, H.X. Wan et al., Development of calculation code for fission product in PWR primary loop. Nuclear Power Eng. **35**, 207–210 (2014).https://doi.org/10.13832/j.jnpe.2014.S2.0207 **(in Chinese)**
3. S.H. Tang, W.F. Liu, J. Xiong et al., Development of calculation code CPFP for fission product in primary loop of pressurized water reactor nuclear power plant. Nuclear Power Eng. **39**, 33–38 (2018). https://doi.org/10.13832/j.jnpe.2018.04.0033 **(in Chinese)**
4. Z.B. Liu, Research of core distribution calculation for CANDU reactor based on neutron equivalence homogenization theory. (2017). (in Chinese)
5. Z.S. Xie, B.H. Yin, Procedure for the calculation of neutron-flux and power distribution in light water reactor fuel assemblies. Nuclear Power Eng. **10**, 194 (1989). **(in Chinese)**
6. Z.L. Bai, Q. Zhou, Z.J. Yang et al., Development on scintillator fiber detect system for on-line measurement of relative neutron flux density in reactor. Atomic Energy Sci. Technol. **51**, 1658–1664 (2017). https://doi.org/10.7538/yzk.2016.youxian.0753 . **in Chinese**
7. T.S. Yang, Y.Q. Shi, Q.F. Zhu et al., Measurement of neutron flux density in reactor with thermal analysis method. Atomic Energy Sci. Technol. **50**, 1630–1633 (2016). https://doi.org/10.7538/yzk.2016.50.09.1629. in Chinese
8. L. Deng, C. Deng, Study on neutron flux density simulation. Nuclear Power Eng. **20**, 210–213 (1999). https://doi.org/10.1017/CBO9781107415324.004in Chinese
9. Z.H. Li, Differences and interrelationships among commonly used neutron flux expressions. China J. Nuclear Sci. Eng. **13**, 278–282 (1993). **(in Chinese)**
10. L.J. Yang, S.Z. Zhao, W. Zhang, Relationship of burnup and neutron emission intensity for spent fuel. Atomic Energy Sci. Technol. **43**, 1106–1109 (2009). **(in Chinese)**
11. L.L. Liu, X.Z. Wu, Y.J. Chen et al., Study of fission dynamics with a three-dimensional Langevin approach. Phys. Rev. C **99**, 1–10 (2019). https://doi.org/10.1103/PhysRevC.99.044614
12. G.X. Dong, Y.J. Chen, X.B. Wang et al., Mass distributions of fission fragments for n+^{233}U reaction investigated by GEF model. Sci. Sin. Physica, Mech. Astron. (2019). https://doi.org/10.1360/sspma-2019-0222
13. Z.A. Wang, J.C. Pei, Y. Liu et al., Bayesian evaluation of incomplete fission yields. Phys. Rev. Lett. **123**, 122501 (2019). https://doi.org/10.1103/PhysRevLett.123.122501
14. H. Tao, J. Zhao, Z.P. Li et al., Microscopic study of induced fission dynamics of Th 226 with covariant energy density functionals. Phys. Rev. C **96**, 1–10 (2017). https://doi.org/10.1103/PhysRevC.96.024319
15. N. Wang, W. Ye, Probing nuclear dissipation with first-chance fission probability. Phys. Rev. C **97**, 1–7 (2018). https://doi.org/10.1103/PhysRevC.97.014603
16. O. Leray, L. Fiorito, D. Rochman et al., Uncertainty propagation of fission product yields to nuclide composition and decay heat for a PWR UO2 fuel assembly. Prog. Nucl. Energ. **101**, 486–495 (2017). https://doi.org/10.1016/j.pnucene.2017.05.033
17. D. Rochman, O. Leray, A. Vasiliev et al., A Bayesian Monte Carlo method for fission yield covariance information. Ann. Nucl. Energy **95**, 125–134 (2016). https://doi.org/10.1016/j.anucene.2016.05.005
18. D.F. da Cruz, D. Rochman, A.J. Koning, Quantification of uncertainties due to ^{235,238}U, ^{239,240,241}Pu and fission products nuclear data uncertainties for a PWR fuel assembly. Nucl. Data Sheets **118**, 531–534 (2014). https://doi.org/10.1016/j.nds.2014.04.126
19. D. Ramos, M. Caamaño, F. Farget et al., Insight into excitation energy and structure effects in fission from isotopic information in fission yields. Phys. Rev. C **99**, 1–11 (2019). https://doi.org/10.1103/PhysRevC.99.024615
20. P. Möller, D.G. Madland, A.J. Sierk et al., Nuclear fission modes and fragment mass asymmetries in a five-dimensional deformation space. Nature **409**, 785–790 (2001). https://doi.org/10.1038/35057204
21. U. Brosa, S. Grossmann, A. Müller et al., Nuclear scission. Nucl. Phys. A **502**, 423–442 (1989). https://doi.org/10.1016/0375-9474(89)90680-5
22. H. Paşca, A.V. Andreev, G.G. Adamian et al., Toward an understanding of the anomaly in charge yield of Mo and Sn fragments in the fission reaction ^{238}U(n, f). Phys. Rev. C **98**, 1–3 (2018). https://doi.org/10.1103/PhysRevC.98.014624
23. C.K. Zheng, H.J. Jiang,, The fission yield of ^{235}U and ^{238}U induced by mono-neutron. China Nuclear Science And Technology Report, 5. (1993). CNKI:SUN:ZHBG.0.1993-00-005. (in Chinese)
24. R. Wigeland, T. Taiwo, H. Ludewig et al., Nuclear fuel cycle evaluation and screening. INL/EXT-14-31465 (2014)
25. V.D. Sevast'yanov, A.S. Koshelev, G.N. Maslov, Investigating the thermal and epithermal neutron spectra in the moderators of nuclear reactors. Instrum. Exp. Techn. **47**, 731–743 (2004). https://doi.org/10.1023/b:inet.0000049691.40579.5e
26. Y.J. Chen, M. Jia, T.J. Liu et al., Calculation of prompt fission neutron spectrum for ^{233}U(n, f) reaction by the semi-empirical method. Chin. Phys. C **38**, 5 (2014). https://doi.org/10.1088/1674-1137/38/5/054001
27. R.D. Kale, India's fast reactor programme: a review and critical assessment advanced fuel development with high breeding ratio. Prog. Nucl. Energ. **122**, 103–265 (2020). https://doi.org/10.1016/j.pnucene.2020.103265
28. A. Zhang, C.Y. Zou, J.H. Wu et al., Radiotoxicity of minor actinides in thermal, epithermal and fast TMSRs with very high burnup. Ann. Nucl. Energy **137**, 107–162 (2020). https://doi.org/10.1016/j.anucene.2019.107162
29. W.C. Hu, B. Liu, X.P. Ouyang et al., Minor actinide transmutation on PWR burnable poison rods. Ann. Nucl. Energy **77**, 74–82 (2015). https://doi.org/10.1016/j.anucene.2014.10.036
30. S.C. Zhou, H.C. Wu, Y.Q. Zheng, Flexibility of ADS for minor actinides transmutation in different two-stage PWR-ADS fuel cycle scenarios. Ann. Nucl. Energy **111**, 271–279 (2018). https://doi.org/10.1016/j.anucene.2017.08.037
31. Arkoma Asko, Huhtanen Risto, Leppänen Jaakko, Peltola Juho, Pättikangas. Timo, Calculation chain for the analysis of spent nuclear fuel in long-term interim dry storage. Ann. Nucl. Energy **119**, 129–138 (2018). https://doi.org/10.2172/809946

32. A.C. Wahl,, Systematics of fission-product yields.Technical Report LA-13928, (2002) https://doi.org/10.2172/809946
33. S. Okumura, T. Kawano, P. Jaffke et al., ^{235}U(n, f) Independent fission product yield and isomeric ratio calculated with the statistical Hauser–Feshbach theory. J. Nucl. Sci. Technol. **55**, 1009–1023 (2018). https://doi.org/10.1080/00223131.2018.1467288
34. A.V. Andreev, G.G. Adamian, N.V. Antonenko et al., Possible explanation of fine structures in mass-energy distribution of fission fragments. Euro. Phys. J. A **22**, 51–60 (2004). https://doi.org/10.1140/epja/i2004-10017-9
35. L.L. Liu, N.C. Shu, T.J. Liu et al., Study on mass distribution of n+^{233}U fission with phenomenological model. Nucl. Phys. Rev. **30**, 374–378 (2013). https://doi.org/10.11804/NuclPhysRev.30.03.374
36. L. Zhu, P.W. Wen, C.J. Lin et al., Shell effects in a multinucleon transfer process. Phys. Rev. C **97**, 1–10 (2018). https://doi.org/10.1103/PhysRevC.97.044614
37. I. Dutt, R.K. Puri, Comparison of different proximity potentials for asymmetric colliding nuclei. Phys. Rev. C **81**, 1–12 (2010). https://doi.org/10.1103/PhysRevC.97.044614
38. N.C. Shu, Y.J. Chen, T.J. Liu et al., Semi-empirical study on the yield energy-dependence of the ^{235}U + n fission. J. Korean Phys. Soc. **59**, 1353–1356 (2011). https://doi.org/10.3938/jkps.59.1353
39. J. Lee, C.S. Gil, Y.O. Lee et al., Calculation of fission product yields for uranium isotopes by using a semi-empirical model. Euro. Phys. J. A **54**, 173 (2018). https://doi.org/10.1140/epja/i2018-12607-2
40. J. Benlliure, A. Grewe, M.D. Jong et al., Calculated nuclide production yields in relativistic collisions of fissile nuclei. Nucl. Phys. A **628**, 458–478 (1998). https://doi.org/10.1016/S0375-9474(97)00607-6
41. A.C. Wahl, Nuclear-charge distribution and delayed-neutron yields for thermal-neutron-induced fission of ^{235}U, ^{233}U and ^{239}Pu and for spontaneous fission of ^{252}Cf. At. Data Nucl. Data Tables **39**, 1–156 (1988). https://doi.org/10.1016/0092-640X(88)90016-2
42. H. Naik, R.J. Singh, R.H. Lyer, Charge distribution studies in the fast-neutron-induced fission of ^{232}Th, ^{238}U, ^{240}Pu and ^{244}Cm. Eur. Phys. J. A **16**, 495–507 (2003). https://doi.org/10.1140/epja/i2002-10122-9
43. H.W. Wiese, Actinide transmutation properties of thermal and fast fission reactors including multiple recycling. J. Alloy. Compd. **271–273**, 522–529 (1998). https://doi.org/10.1016/S0925-8388(98)00141-8
44. L. Zhang, Y.W. Yang, Y.G. Fu et al., Development and validation of the code COUPLE3.0 for the coupled analysis of neutron transport and burnup in ADS. Nucl. Sci. Tech. **29**, 124 (2018). https://doi.org/10.1007/s41365-018-0471-4
45. W.J. Maeck, A.L. Erikson, R.L. Tromp, Fast reactor fission yields for ^{241}Pu and relative fission product isotopic data for ^{239}Pu irradiated in Row-4 of EBR-II. Exxon Nuclear Idaho Co.. (1980)
46. W.J. Maeck, R.L. Eggleston, A.L. Erikson et al., *Fast Reactor Fission Yields for ^{240}Pu and ^{242}Pu* (Allied Chemical Corp, Morristown, 1979)
47. R. Brissot, J. Crançon, Ch. Ristori et al., istributions isotopiques des gaz rares et de leurs precurseurs dans la fission thermique de ^{239,241}Pu: Etude de l'effet "pair-impair''. Nucl. Phys. A **282**, 109–124 (1977). https://doi.org/10.1016/0375-9474(77)90174-9
48. W.A. Myers, M.V. Kantelo, R.L. Osborne et al., Fast Neutron Fission of ^{240}Pu. Phys. Rev. C **18**, 1700 (1978). https://doi.org/10.1103/PhysRevC.18.1700
49. H. Naik, A.G.C. Nair, P.C. Kalsi et al., Absolute fission yields in the fast neutron induced fission of 99.9997 Atom% pure ^{238}U using track etch-cum gamma spectrometric technique. Radiochimica Acta **75**, 69–76 (1996). https://doi.org/10.1524/ract.1996.75.2.69
50. J.E. Gindler, L.E. Glendenin, D.J. Henderson et al., Mass distributions in monoenergetic-neutron-induced fission of ^{239}Pu. Phys. Rev. C **27**, 2058–2062 (1983). https://doi.org/10.1103/PhysRevC.27.2058
51. J.K. Dickens, J.W. McConnell, Fission product yields for thermal-neutron fission of plutonium-239. Nucl. Sci. Eng. **73**, 42–55 (1980). https://doi.org/10.13182/NSE80-A18707
52. S. Nagy, K.F. Flynn, J.E. Gindler et al., Mass distributions in monoenergetic-neutron-induced fission of ^{238}U. Phys. Rev. C **17**, 163–171 (1978). https://doi.org/10.1103/PhysRevC.17.163
53. L.E. Glendenin, J.E. Gindler, D.J. Henderson et al., Mass distributions for monoenergetic-neutron-induced fission of ^{235}U. Phys. Rev. C **24**, 2600–2605 (1981). https://doi.org/10.1103/PhysRevC.24.2600
54. A.I. Sergachev, N.P. Dyachenko, A.M. Kovalev et al., Influence of excitation energy on the mass and kinetic energy distributions of ^{233}U fission fragments. Sov. J. Nuclear Phys.-USSR **16**, 266 (1973)
55. W.J. Maeck, *Fast Reactor Fission Yields for ^{233}U, ^{235}U, ^{238}U, ^{239}Pu, and Recommendations for the Determination of Burnup on FBR Mixed Oxide Fuels* (Allied Chemical Corp, Morristown, 1975)
56. R.B. Strittmatter, B.W. Wehring, Fragment atomic-number identification using a gas ionization chamber in fission yield measurements. Nucl. Instrum Methods **166**, 473–481 (1979). https://doi.org/10.1016/0029-554X(79)90537-8
57. R. Brissot, J. Crançon, Ch. Ristori et al., Distributions isotopiques des gaz rares dans la fission par neutrons thermiques de ^{235}U et ^{233}U. Nucl. Phys. A **255**, 461 (1975). https://doi.org/10.1016/0375-9474(75)90693-4
58. S.J. Balestrini, R. Decker, H. Wollnik et al., Independent yields of Rb and Cs isotopes from thermal-neutron induced fission of ^{235}U. Phys. Rev. C **20**, 2244–2248 (1979). https://doi.org/10.1103/PhysRevC.20.2244
59. W. Reisdorf, J.P. Unik, H.C. Griffin et al., Fission fragment K x-ray emission and nuclear charge distribution for thermal neutron fission of ^{233}U, ^{235}U, ^{239}Pu and spontaneous fission of ^{252}Cf. Nucl. Phys. A **177**, 337–378 (1971). https://doi.org/10.1016/0375-9474(71)90297-1
60. K. Wang, B. Liu, W.C. Hu et al., The effect to the nuclear reactor after the actinide nuclides added to the nuclear fuel. Chin. J. Nucl. Sci. Eng. **32**, 205–211 (2012). (**in Chinese**)
61. H.J. Amster, The Wigner-Wilkins calculated thermal neutron spectra compared with measurements in a water moderator. Nucl. Sci. Eng. **2**, 394–404 (1957). https://doi.org/10.13182/nse57-a25404
62. L. Cranberg, G. Frye, N. Nereson et al., Fission neutron spectrum of ^{235}U. Phys. Rev. **103**, 662–670 (1956). https://doi.org/10.1103/PhysRev.103.662
63. T. He, P. Zheng, J. Xiao, Measurement of the prompt neutron spectrum from thermal-neutron-induced fission in^{235}U using the recoil proton method. Nucl. Sci. Tech. **30**, 112 (2019). https://doi.org/10.1007/s41365-019-0633-z
64. J.A.D. Salomé, F. Cardoso, C.E. Velasquez et al., VHTR, ADS, and PWR spent nuclear fuel analysis. Procedia Chem. **21**, 255–262 (2016). https://doi.org/10.1016/j.proche.2016.10.036
65. J.D. Chen, F.X. Yu, K.Y. Cai et al., *Daya Bay Nuclear Power Station System and Operation* (Atomic Energy Press, Beijing, 1995). (**in Chinese**)
66. J.R. Burns, R. Hernandez, K.A. Terrani et al., Reactor and fuel cycle performance of light water reactor fuel with ^{235}U enrichments above 5%. Ann. Nucl. Energy **142**, 107423 (2020). https://doi.org/10.1016/j.anucene.2020.107423

67. Private communication with Engineer C.S. Zhou at Daya Bay nuclear power plant in February, 2020
68. D.Y. Cui, S.P. Xia, X.X. Li et al., Transition toward thorium fuel cycle in a molten salt reactor by using plutonium. Nucl. Sci. Tech. **28**, 152 (2017). https://doi.org/10.1007/s41365-017-0303-y
69. W.F. Wang, Nuclear reactor physics advanced operations training materials. JNPC **169**(2017)
70. A. Trkov, R. Capote, V.G. Pronyaev, current issues in nuclear data evaluation methodology: ^{235}U prompt fission neutron spectra and multiplicity for thermal neutrons. Nucl. Data Sheets **123**, 8–15 (2015). https://doi.org/10.1016/j.nds.2014.12.003